ISSN 1023-1935, Russian Journal of Electrochemistry, 2023, Vol. 59, No. 12, pp. 1092–1101. © Pleiades Publishing, Ltd., 2023.
Russian Text © The Author(s), 2023, published in Elektrokhimiya, 2023, Vol. 59, No. 12, pp. 856–866.

The Effect of the Synthesis Method of the Layered Manganese Dioxide on the Properties of Cathode Materials for Aqueous Zinc-Ion Batteries

M. A. Kamenskii[a], A. Yu. Popov[a], S. N. Eliseeva[a], and V. V. Kondratiev[a, *]

[a] *Institute of Chemistry, St.-Petersburg State University, St.-Petersburg, Russia*

**e-mail: vkondratiev@mail.ru*

Received November 25, 2022; revised May 14, 2023; accepted June 6, 2023

Abstract—The dependence of physico-chemical, structural, and electrochemical properties of cathode materials for aqueous zinc-ion batteries based on the manganese dioxide with birnessite-type structure on the conditions of the MnO_2 hydrothermal synthesis are analyzed. The manganese oxides obtained are capable of the reversible zinc ion intercalation into their crystal lattice because of large interlayer distances. Two approaches to the synthesis are considered: a reaction between manganese sulfate and potassium permanganate at 160°C (MnO_2-I) and hydrothermal treatment of potassium permanganate solution at 220°C (MnO_2-II). From the structural analysis, both methods are shown to allow obtaining the birnessite-type manganese dioxide. At the same time, the electrochemical properties of the cathodes obtained differ in the prototypes of aqueous zinc-ion batteries. The MnO_2-II-based material demonstrated higher initial specific capacity (180 mA h g^{-1} at the current density of 0.3 A g^{-1}), while its cyclic stability is by 40% lower than that for the MnO_2-I-based material. This can be explained by higher surface area and lower crystallinity of the active material.

Keywords: manganese dioxide, hydrothermal synthesis, aqueous zinc-ion batteries, electrochemical performance

DOI: 10.1134/S1023193523120066

INTRODUCTION

In the recent years, the development of new types of practicable and environment-friendly current sources is a hot topic. To date, lithium-ion batteries are most widely used; however, they have disadvantages. In particular, the latter are: (a) the toxicity of cathodic materials containing cobalt oxide and its based mixed oxides; (b) explosion risk because of using of flammable solvents based on organic carbonates; and (c) a limited lithium amount in the Earth resources and, as a consequence, the lithium high price. The alternative current sources are sodium-ion batteries [1], as well as multivalent metal–ion systems [2, 3]. Among the latter, aqueous zinc-ion batteries are of special interest because of the zinc non-toxicity, low price, the possibility of using aqueous electrolyte solutions, as well as low redox-potential of the Zn/Zn^{2+} transition (−0.76 V vs. H_2/H^+) [4].

The cathodic materials thinkable for the zinc-ion batteries make a wide variety of inorganics: vanadium and manganese oxides, analogs of the Prussian blue, the transition metal dichalcogenides [5]. Among them, the manganese oxides, in particular, the manganese dioxide has the largest energy density for the transition at the potentials 1.3–1.5 V vs. Zn/Zn^{2+}; also, the MnO_2 is inexpensive and environment-friendly [6–10]. The manganese dioxide can form a variety of structural and polymorphous modifications: the tunnel (α-, β-, γ-MnO_2), spinel (ε-, R-MnO_2, $MeMn_2O_4$), and layered ones (δ-MnO_2) [11]. One of the most attractive for using in the zinc-ion batteries is the MnO_2 layered modification with the birnessite-type structure (or δ-MnO_2), because of its large interlayer distance (≈7 Å). This facilitates the zinc ion transport into the oxide crystal lattice, which improves the electrochemical properties of cathodic materials [12–14].

Depending on the synthesis conditions, one can obtain different manganese dioxide polymorphous modifications. Most often, a hydrothermal synthesis is used, in which the process conditions are varied [15–17]. However, upon changing the medium acidity or temperature, the tunnel modification β-MnO_2 can be obtained in addition to the δ-MnO_2 [18]. Moreover, the morphology and, as a consequence, the cathodic-material electrochemical properties are also changed depending on the synthesis conditions.

In this work, we aimed at synthesizing the manganese dioxide with layered structure (δ-MnO_2) with different methods, as well as studying the effect of the reaction mixture composition and synthesis conditions on both the cathode-material morphological parameters and electrochemical properties in a zinc-ion battery prototype. Depending on the solution composition and temperature in the hydrothermal synthesis, we observed different crystallinity degree of the prepared oxides, which, in its turn, affects the cathodic-materials' electrochemical properties, in particular, their stability during long-term cycling. Of special interest is the study of electrochemical properties of the material obtained by hydrothermal treatment of $KMnO_4$ solution because it has not been studied as a cathode material for the zinc-ion batteries.

EXPERIMENTAL

The δ-MnO_2 powders were obtained by the hydrothermal synthesis with the using of the synthetic procedures disclosed earlier [12, 18]. In the synthesis, potassium permanganate $KMnO_4$ (reagent grade) and manganese sulfate $MnSO_4$ (analytical grade, LenReaktiv, Russia) were used.

The Synthesis Involving $KMnO_4$ and $MnSO_4$ (Method I)

For the synthesis, we prepared 0.036 M $KMnO_4$ solution by dissolving potassium permanganate (0.2878 g) in 50 mL of deionized water. The obtained solution was added by manganese sulfate $MnSO_4$ (0.0458 g), so that the component molar ratio came to 6:1, in compliance with work [12]. The obtained solution was agitated with a magnetic stirrer for 30 min, then it was transferred into a steel autoclave. The synthesis was carried out at 160°C for 12 h. The obtained black powder was washed with deionized water by using a centrifuge (the rotation velocity was 4500 min^{-1}; the time, 5 min), then dried in vacuum at 55°C for 18 h. The reaction yield was 60%. In what follows, the obtained material is designated as MnO_2-I.

Hydrothermal Treatment of $KMnO_4$ (Method II)

We prepared 0.025 M potassium permanganate solution by dissolving of 0.200 g of the salt in 50 mL of water under agitation for 30 min, then it was placed into a steel autoclave. The synthesis was carried out at a temperature of 220°C for 24 h [18]. The obtained black powder was washed with deionized water by using a centrifuge (the rotation velocity was 4500 min^{-1}; the time, 5 minн), then dried under vacuum at 60°C for 20 h. The reaction yield was ≈98%. In what follows, the obtained material is designated as MnO_2-II.

Characteristics of Obtained Materials

The phase composition of the synthesized oxides was analyzed by X-ray diffraction over the 10°–70° angle range by using CuK_α radiation ($\lambda = 0.15418$ nm) with a Bruker-AXS D8 DISCOVER diffractometer (Germany) at a scanning step of 0.02°. The obtained particles' morphology was studied using scanning electron microscopy method with a SUPRA 40VP scanning electron microscope (Carl Zeiss, Germany). The elemental analysis of the obtained material surface was carried out by energy dispersive X-ray analysis. The thermal analysis was carried out by thermogravimetry, with the using of a Netzsch TG 209 F1 Libra thermomicrobalance (Germany).

The Cathodic Materials' Preparation and Testing

The synthesized materials were mixed in agate mortar with amorphous carbon (carbon black, Timcal Inc., Belgium) and polyvinylidene fluoride (a binder) dissolved in N-methyl-2-pyrrolidone (Aldrich, US) at a ratio of 70 : 20 : 10. The obtained mixture was mixed in the mortar for 20 min. The obtained suspension was applied to titanium foil ($l = 20$ μm) using an applicator pipet (the film thickness 150 μm). The materials were dried in vacuum at 50°C within 24 hours, then rolled up for the better material hold-down to the conductive substrate. The material load on the electrode was ≈1–1.5 mg cm^{-2}.

For electrochemical testing, we assembled prototypes of zinc-ion batteries in the CR2032-unit-size cells, where zinc-metal was the anode; 2 M $ZnSO_4$/0.1 M $MnSO_4$ (LenReaktiv, Russia) aqueous solution, the electrolyte; Whatman GF/A glass-fiber, the separator. The testing (by the galvanostatic charging–discharging) was carried out with a CT–4008 automated galvanostatic workstation (Neware Co., China) over the 1.0–1.8 V voltage range (vs. Zn/Zn^{2+}) with the 0.1–5.0 A g^{-1} currents. In the studies by the cyclic voltammetry and electrochemical impedance spectroscopy methods, a Biologic BCS-805 potentiostat–galvanostat (Biologic, France) was used. Cyclic voltammograms were taken at a potential scanning rate of 0.1 mV s^{-1} over the $E = 1.0$–1.8 V range. The electrochemical impedance spectra were recorded over the 10 kHz–0.1 Hz frequency range, at an amplitude of 5 mV, during the discharging at $E = 1.48$, 1.38, and 1.30 V. All electrochemical measurements were carried out at the room temperature (22 ± 2°C).

RESULTS AND DISCUSSION

The primary characterization of the prepared materials by the X-ray diffraction analysis showed that regardless of the solution composition and synthesis temperature we obtained the potassium-doped manganese dioxide with birnessite-type structure (Fig. 1). This result correlates with the literature data concern-

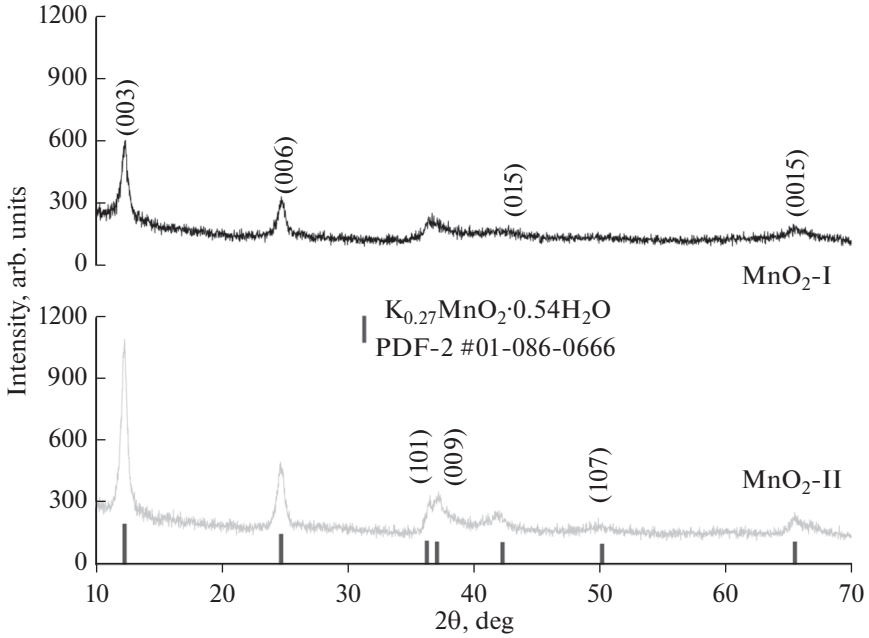

Fig. 1. X-ray diffraction patterns for manganese dioxide MnO_2 synthesized by different methods.

ing X-ray diffraction [12, 18, 19] (the diffraction card 00-080-1098), which confirmed the reproducibility of both procedures. In the diffraction patterns we see two intense peaks at 12.3° and 24.7° corresponding to the planes (0,0,3) and (0,0,6), as well as paired peaks characteristic of layered crystal structures. The presence of potassium ions in the structure is connected with the $KMnO_4$ excess in reaction systems; in addition, they keep the manganese dioxide layers at fixed distances. The elemental composition of the obtained product approaches that found earlier for the manganese dioxide with similar structure [19]; it can be written as $K_{0.27}MnO_2{\cdot}0.54H_2O$, in compliance with the (PDF−2 #01-086-0666) card.

In addition, by comparing the peak intensities one can conclude on the difference in the powder crystallinity degree: we see that in the case of the MnO_2-I powder the peaks are less intense than those relating to MnO_2-II, and somewhat broader. This evidenced, even if indirectly, that the material obtained by the procedure II has a better crystallinity.

The powder morphology was studied by the scanning electron microscopy (Fig. 2). We see that the MnO_2-I sample demonstrated a trend to the formation of large-size agglomerates (≈90 μm) in which separate crystals are barely discernible (Fig. 2a); when coming to larger scale, no well pronounced crystal fragments are present, which confirms a more amorphous structure (Fig. 2b). By contrast, for the MnO_2-II sample, we clearly see that the agglomerates consist of separate smaller particles sized 1.5 to 6 μm which remained being detectable even at further magnifications (Fig. 2d, 2e). Nonetheless, both materials consisted of randomly oriented layered structures resembling nanoflowers or nanoleaves (Fig. 2c, 2f). This morphology confirmed the manganese dioxide layered structure. Thus, the starting chemicals and synthesis conditions (in particular, temperature) affected the micromorphology of the obtained materials.

The thermal analysis of synthesized samples is shown in Fig. 3. We see that at temperatures below 150°C the samples lost about 7% of their mass in air and 8% of their mass in argon atmosphere because of the adsorbed and crystallization water evaporation. We see from the differential mass-loss profiles that the peaks connected with the evaporation of different forms of water are practically indistinguishable, which evidenced both the closeness of water evaporation temperatures and small content of the crystallization water in the material, which is in good agreement with the data of X-ray diffraction. At $T > 350$°C in argon atmosphere we observed further decrease of mass, which can be connected with the material destruction (the Mn^{4+} partial reduction) [20].

The electrochemical properties of electrode materials were studied in the 2 M $ZnSO_4$/0.1 M $MnSO_4$ aqueous solution in a zinc-ion battery prototype. The adding of Mn^{2+} cations into the electrolyte was caused by the necessity to suppress the MnO_2-cathode partial dissolution observed in the course of cycling [21, 22]. In Fig. 4 we show cyclic voltammograms for both types of cathodic materials. In cyclic voltammograms we observed two pairs of peaks at $E_1 = 1.57/1.25$ V and $E_2 = 1.61/1.37$ V. According to literature data, the first pair of peaks corresponds to the zinc cation reversible intercalation into δ-MnO_2 structure. During the dis-

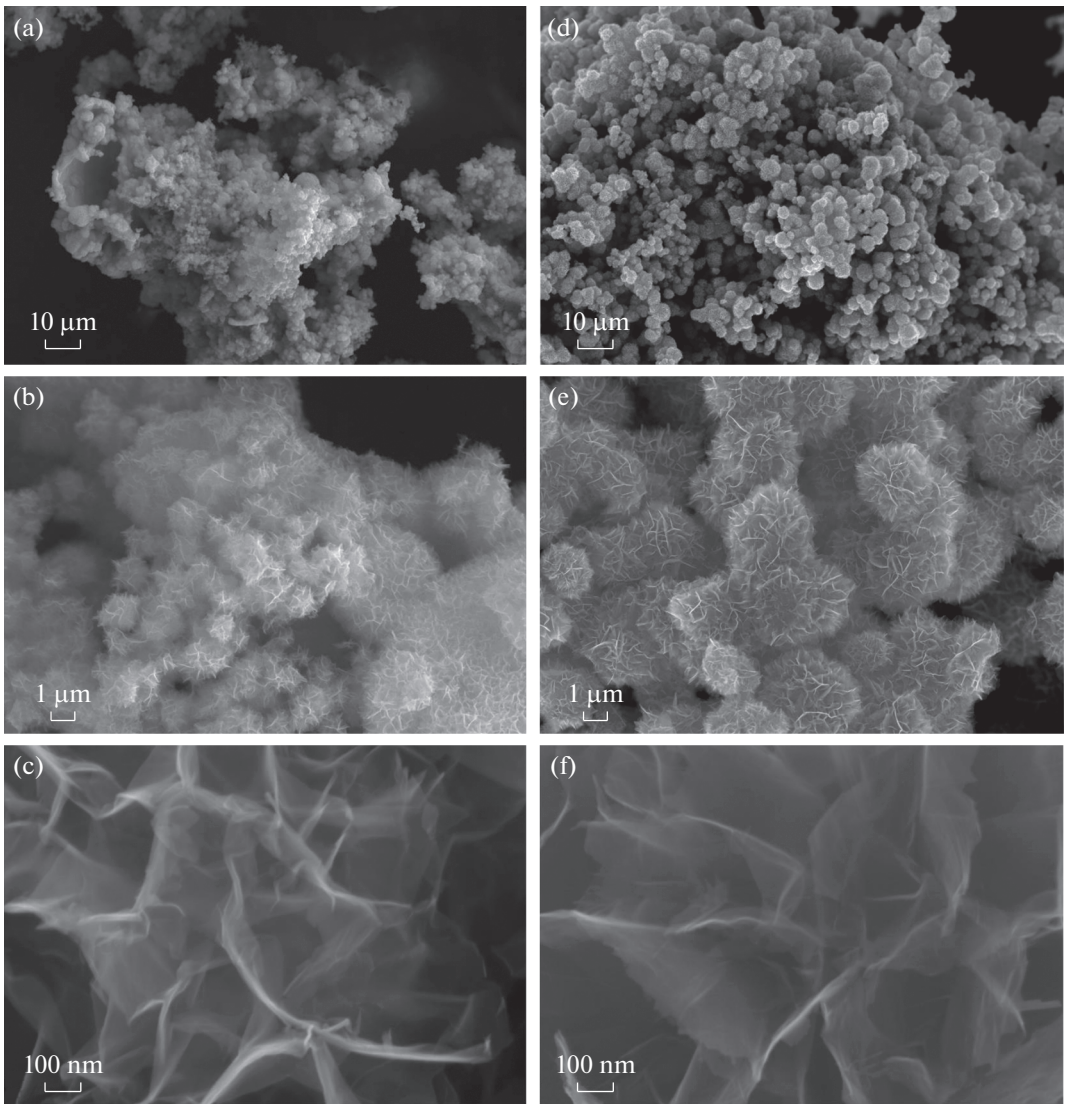

Fig. 2. Scanning electron microphotographs of manganese dioxide powders synthesized by the method I (a–c) and II (d–f), at different magnifications.

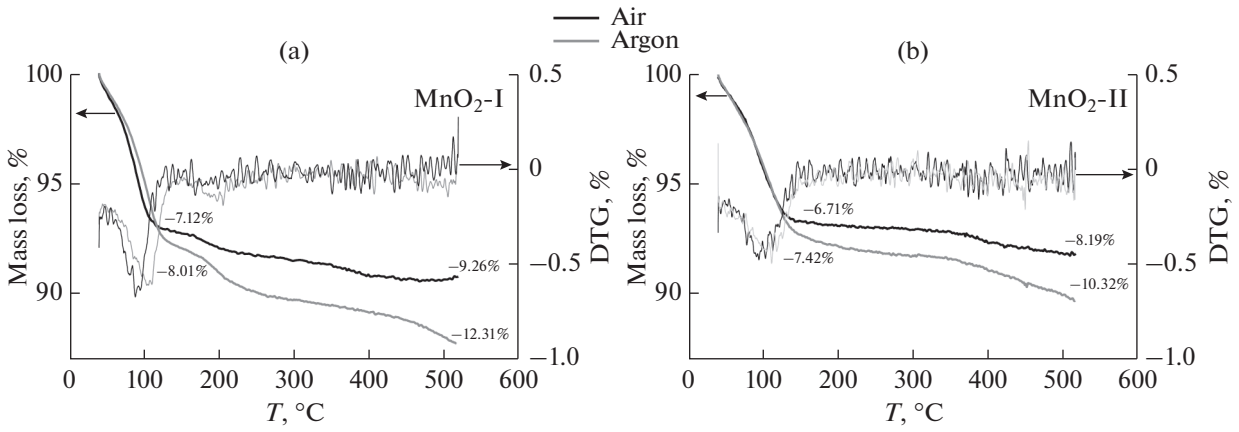

Fig. 3. Thermogravimetric curves and DTG-dependences for manganese dioxide samples obtained by the method I (a) and II (b).

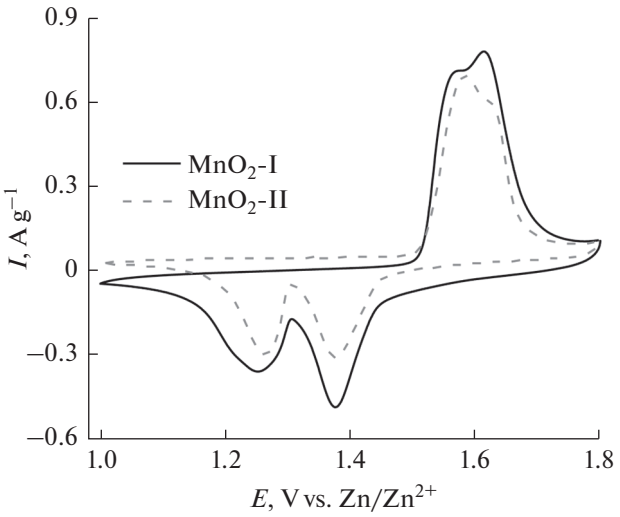

Fig. 4. Cyclic voltammograms (the 5th cycle) for the MnO_2-based cathode materials obtained by different methods; the potential scanning rate $v = 0.1$ mV s^{-1}.

charge, the injection process is connected with the formation of the zinc basic salt $Zn_4(OH)_6SO_4$; the other peak pair relates to the processes of the proton intercalation and deintercalation (H^+ is present in the aqueous solution) [16, 26].

The comparing of the cyclic voltammograms showed that at low potential scanning rate both materials have nearly equal specific current values, hence, the specific capacities. However, in the course of further cycling of the materials, the following trends came to light (Fig. 5). For the MnO_2-I sample, we observed fast growth of the anodic and cathodic currents from the 1st cycle to the 5th one; then, a slower growth until the 20th cycle; afterwards, the current stabilized (Fig. 5a). The current growth can be explained both by more complete working-out of the electrode material and by the side-process of the MnO_x phase deposition from the electrolyte solution [21]. The MnO_2-II sample synthesized from pure $KMnO_4$ demonstrated the growth of the anodic current after the 1st cathodic cycle, with a very small change in the cathodic curve. After the 5th cycle, the current decayed but insignificantly, with its subsequent stabilizing (Fig. 5b). This behavior can be explained by the difference in the starting materials' crystallinity: in the more amorphous material, the intercalation and the concomitant process of the MnO_x deposition onto the cathode surface occur easier than in the highly crystallized oxide. This effect is widely cited in connection with the vanadium-oxide-based cathode materials [23, 24]; it was also observed with the MnO_2-based cathodes [19, 25]. For both materials, in their cyclic voltammograms the anodic peaks shifted toward positive potentials; the cathodic ones, toward a decrease on the overvoltage. Also, well-separated anodic peaks became less pronounced with the increasing of cycle number; instead, a broad anodic peak appeared in the curves.

The cathode materials' functional properties, namely, the specific discharge capacity and its dependence on the current density and the cycle number were studied by the method of galvanostatic charging and discharging (Fig. 6). In Fig. 6a we show dependences of the capacity on the discharging current for the two types of material. We see that the initial capacity of the MnO_2-II (222 mA h g^{-1}) is practically twice as large as that of the MnO_2-I material (103 mA h g^{-1} for the 1st cycle). Nonetheless, for the cathode prepared after the procedure I, at low currents we observed a growth of the specific capacity under the constant current density, which is due to the MnO_x

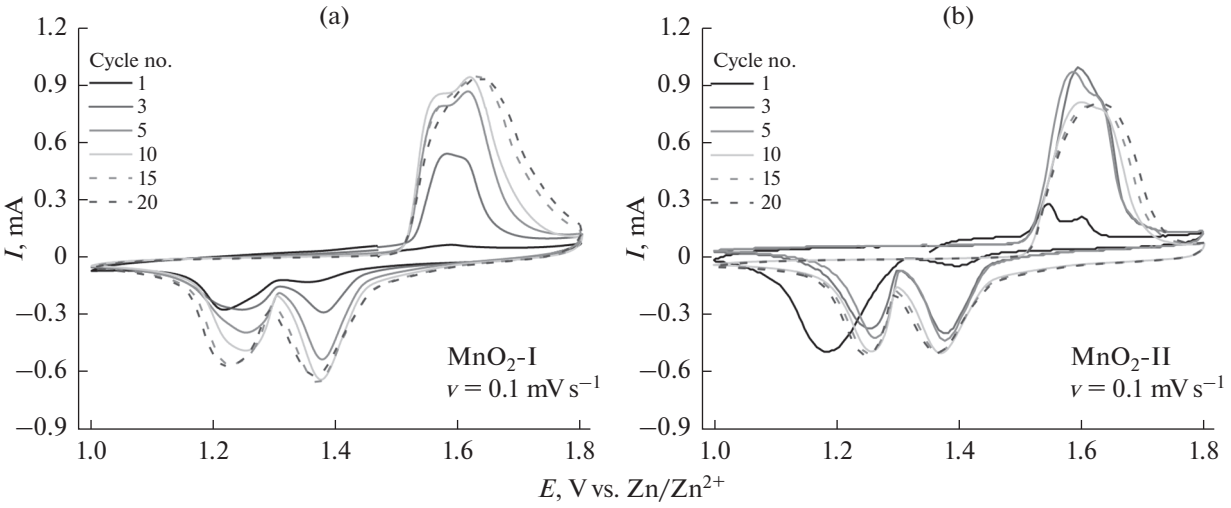

Fig. 5. Cyclic voltammograms for the MnO_2-based cathode materials obtained by the method I (a) and II (b) depending on the cycle number; the potential scanning rate $v = 0.1$ mV s^{-1}.

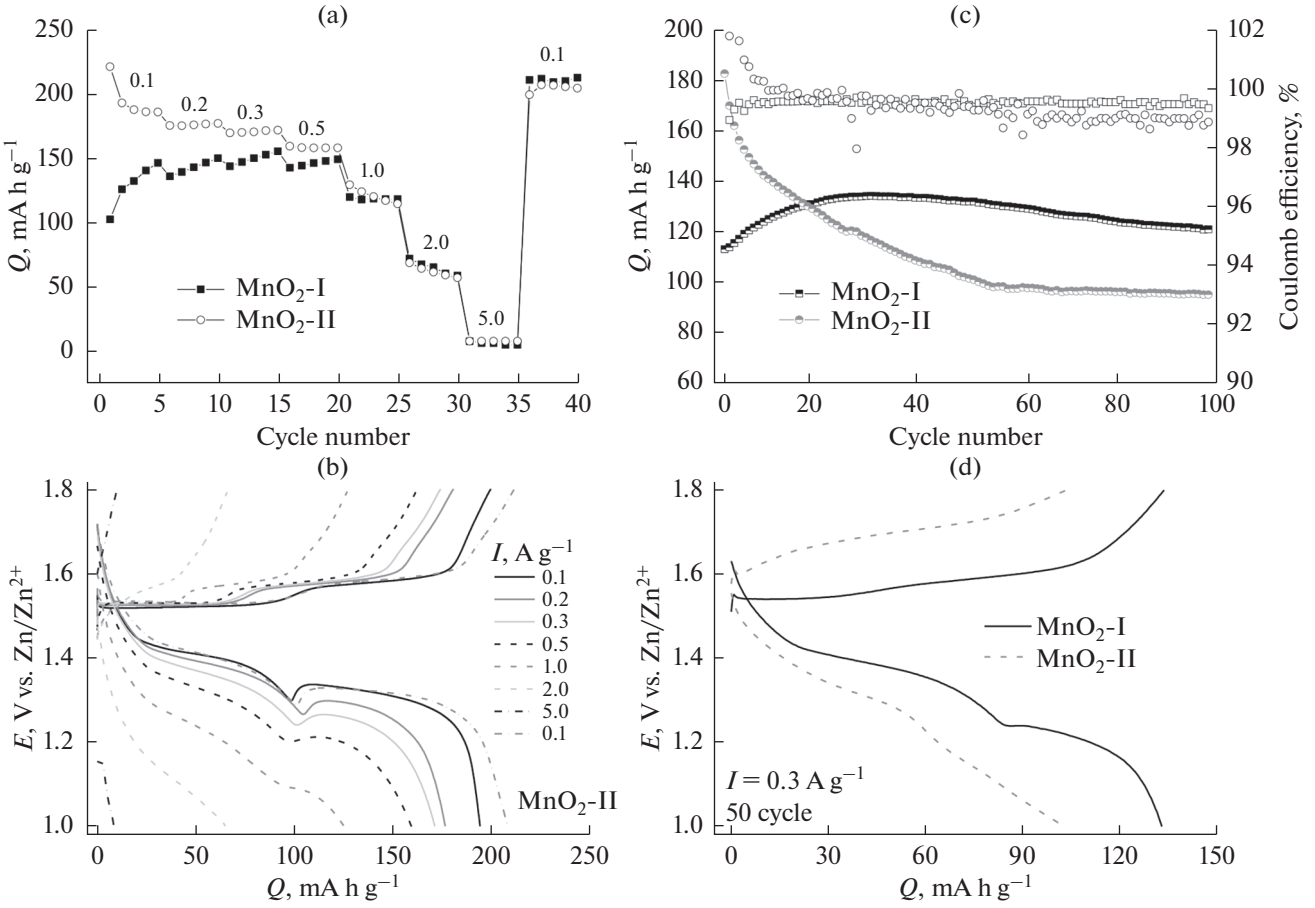

Fig. 6. Functional properties of δ-MnO_2//Zn prototypes: dependence of specific capacity on the discharge current (a), cyclability at the current of 0.3 A g^{-1} (c), charging–discharging curves for MnO_2-cathode obtained by the procedure II (b) and for different materials at the current of 0.3 A g^{-1} (d).

additional deposition from the electrolyte solution. The specific capacities of the materials are comparable over the 0.5–5.0 A g^{-1} current density range.

Of special interest was the studying of the electrochemical response of the MnO_2-II-cathode as a new material for the zinc-ion batteries. The charging–discharging curves at different current densities are presented in Fig. 6b. At lower currents, the discharging curves show two well pronounced plateaus at $E = 1.4$ V and $E = 1.28$ V; they correspond to the H^+ and Zn^{2+} ion intercalation, respectively [16, 26]. In the charging curves, we observed two plateaus at $E \approx 1.55$ V, corresponding to the processes of the zinc ion and proton extraction to the solution. The plateaus' overvoltages correlate well with the peaks in cyclic voltammograms. Upon the increasing of the current from 1 to 5 A g^{-1} the plateaus became less pronounced because of the process high rate and the active material lesser working-out.

The cyclability at the current of 0.3 A g^{-1} is shown in Fig. 6c. For the more amorphous material, the initial capacity came to 113.6 mA h g^{-1}; for the crystalline oxide, to 183.3 mA h g^{-1}. Nonetheless, at long-term cycling, the MnO_2-I showed, firstly, a growth of the capacity up to 134.7 mA h g^{-1} for 30 cycles, then, a decay by 10% from the maximal value. In the case of MnO_2-II, despite the presence of the $MnSO_4$ additive in the solution, the process of MnO_x deposition gave no any significant positive effect: we observed, firstly, a sharp decrease (for 25 cycles), then a smooth fall of the capacity that was stabilized at the 60th cycle; eventually, only 52% of the initial capacity has been retained. The Coulomb efficiency for both materials approached 100%.

The difference of the two materials is clearly seen in the charging–discharging curves. For the amorphous manganese oxide, we observed two poorly resolved plateaus in the charging curve at $E = 1.56$ V and $E = 1.60$ V; in the discharging one, two corresponding plateaus at $E = 1.37$ and 1.22 V. The kink of the curve at $E = 1.24$ V is due to the change in the solution pH caused by the proton injection at the 1st discharge plateau and beginning of the Zn^{2+} ion intercalation [14, 27], as well as a parallel process of hydroxozinc-

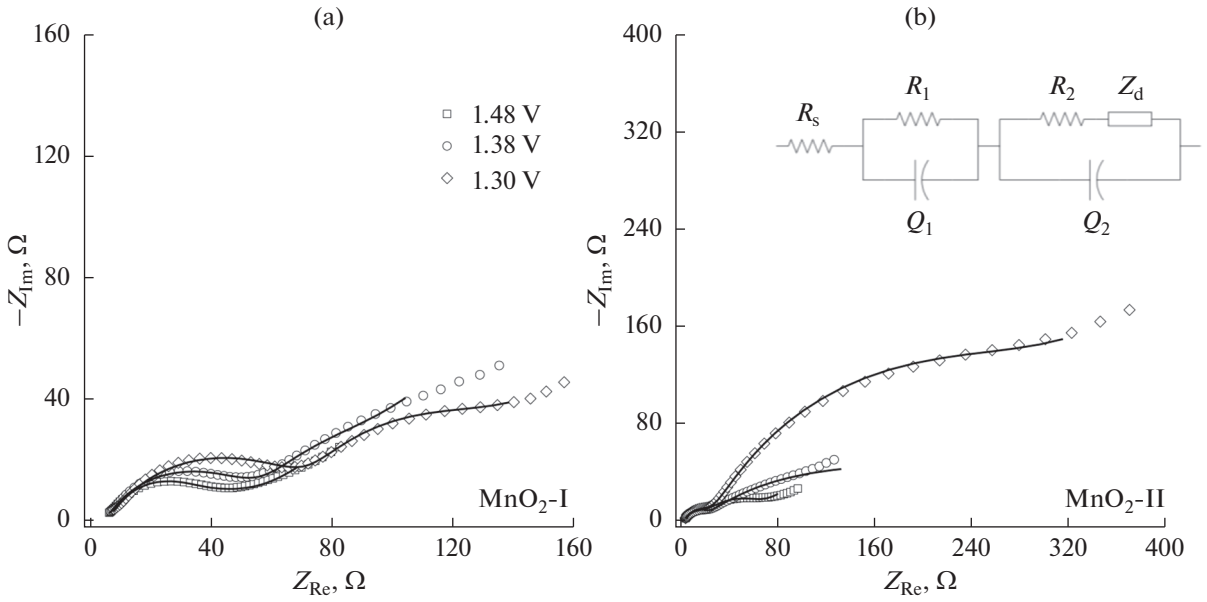

Fig. 7. Impedance spectra for the MnO_2//Zn-cells based on MnO_2-I (a) and MnO_2-II (b), obtained at different voltages during discharge after 20 cycles at the current of 0.3 A g^{-1}. Insert: equivalent circuit; points in the plots—experimental data, lines—calculated impedance spectra corresponding to the equivalent circuit.

sulfate [$Zn_4(OH)_6SO_4$] electrochemically inert layer formation at the electrode surface [28]. For the crystalline MnO_2 the charging and discharging plateaus are poorer pronounced, the electrode polarization is larger than for the more amorphous material. This can be connected with the ever-increasing charge transfer resistance in the cathodic material MnO_2-II and the simultaneously decreasing rate of the ion diffusion into the crystal lattice.

To evaluate the kinetic, in particular, diffusion limitations, we used the electrochemical impedance spectroscopy. In Fig. 7 we show spectra for the two materials, taken during the discharge at the cell voltages approaching the redox-transition potentials: 1.48, 1.38, and 1.30 V. We see that for the MnO_2-I material the spectrum form depended but weakly on the voltage: we observed two semicircumferences at moderate and low frequencies, and a linear segment with a slope of 45° corresponding to diffusion limitations. The impedance spectrum form can be described satisfactorily by involving the equivalent circuit given in literature [14, 29, 30]. In this circuit, the interphase resistance R_1 corresponds to the zinc anode/electrolyte interface; the resistance R_2 is formed at the cathode/electrolyte interface or it is determined by the zinc anode and cathode material in aggregate; the diffusion resistance Z_d corresponds to the ion intercalation into the MnO_2-cathode structure [14].

The impedance spectra for the MnO_2-II material can be described by the same equivalent circuit; however, it is to be noticed that the transition from semicircumference to the linear segment is less pronounced. Also, the semicircumference diameter increased markedly upon the passing from $E = 1.38$ V to $E = 1.30$ V.

When the spectra have been analyzed by the method of equivalent circuits (the results of the analysis are given in Table 1), the resistance R_1 was found to approach 20 Ω, irrespective of the cell voltage other

Table 1. Calculated parameters of impedance spectra for Zn//MnO_2 cells by the equivalent circuit (Fig. 7) depending on the applied voltage

Sample	E, V	R_s, Ω	R_1, Ω	Q_1, F s^{n-1}	n	R_2, Ω	Q_2, F s^{n-1}	n	Z_d, Ω $s^{-1/2}$
MnO_2-I	1.48	3.40	16.87	8.73×10^{-5}	0.90	40.22	3.35×10^{-3}	0.40	22.41
	1.38	5.09	17.98	1.76×10^{-4}	0.89	50.74	9.53×10^{-3}	0.68	49.93
	1.30	5.75	70.90	2.27×10^{-4}	0.88	62.22	3.31×10^{-3}	0.64	26.43
MnO_2-II	1.48	2.22	21.80	2.07×10^{-4}	0.74	45.57	1.03×10^{-3}	0.68	29.13
	1.38	3.86	16.64	3.69×10^{-5}	0.89	41.16	2.90×10^{-3}	0.62	57.61
	1.30	2.90	21.89	8.41×10^{-5}	0.79	226.7	1.33×10^{-3}	0.77	100.2

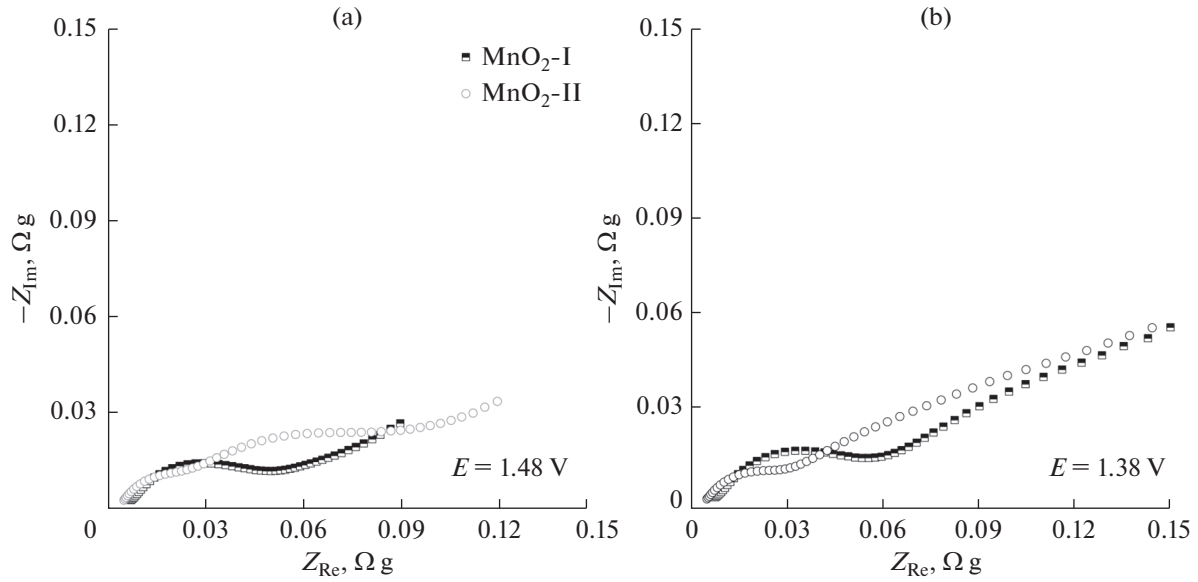

Fig. 8. Impedance spectra for the MnO_2//Zn-cells, normalized per electroactive component mass, obtained at $E = 1.48$ V (a) and $E = 1.38$ V (b).

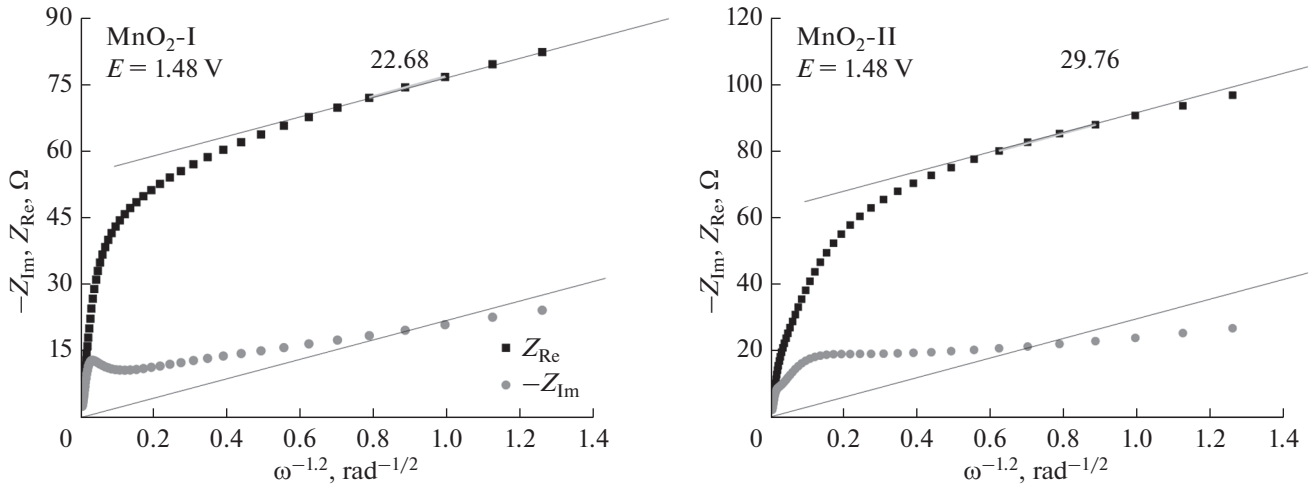

Fig. 9. Dependences Z_{Re}, $-Z_{Im}-\omega^{-1/2}$ for the MnO_2//Zn-cells, obtained at $E = 1.48$ V.

than $E = 1.30$ V for MnO_2-I, prompting suggestions that this resistance corresponds to the same interface, in particular, the zinc anode. The abrupt jump at $E = 1.30$ V for MnO_2-I can be explained by the cell complete passivation upon the deposition of the double salt hydroxozincsulfate. The interface resistance R_2 demonstrated different trends: at $E = 1.48$ V its value is somewhat less than for the MnO_2-I material, it increased with the increasing of the potential. For MnO_2-II, R_2 increased drastically at $E = 1.30$ V, which can be connected with the formation of a non-conducting phase at the electrode surface. When the spectra were counterposed with the active material mass, it was found that the trends to the resistance change have been retained (Fig. 8).

Additionally, we analyzed segments of the curves at lower frequencies, in order to estimate the Warburg diffusion resistance that can appear upon the H^+ and Zn^{2+} ions intercalation into the cathode-material crystal lattice.

The analysis was carried out not only by the equivalent circuit (see Table 1) but also involving the Z_{Re}, $-Z_{Im}-\omega^{-1/2}$ dependences (Fig. 9). With $E = 1.48$ V, we see that the values of the diffusion impedance and Warburg constants obtained by different ways correlate well. For the MnO_2-I material the Z_d

values are lower than for the MnO_2-II, which points to a facilitate ion transport into the structure of the more amorphous material; this effect has been reported in work [25].

CONCLUSIONS

In this work, we made it clear that the conditions of the MnO_2 hydrothermal synthesis, in particular, the reaction mixture composition and temperature, affected the sample crystallinity and micromorphology, the nanostructure being kept unchanged. The hydrothermal treatment of the potassium permanganate solution produced material with larger degree of crystallinity, whereas the product of the manganese permanganate and sulfate interaction showed a pronounced amorphousness.

The difference in the crystallinity affected functional properties of prototypes of the zinc-ion batteries, in particular, the capacity stability upon a long-term cycling. We showed, using different electrochemical methods, that the initial specific capacity of the better crystallized oxide is superior to that of the more amorphized material. However, upon the zinc solvated cation intercalation the material exerted irreversible changes and degraded readily, thus showing only 52% of the initial capacity after 100 charging–discharging cycles at a current density of 0.3 A g^{-1}. Under similar cycling conditions, the more amorphous material retained 90% of the capacity maximal value. The reason therefor may be the ion slower diffusion into the crystal lattice of the better crystallized material, which also follows from the impedance spectra.

ACKNOWLEDGMENTS

The studies by using the scanning electron microscopy, X-ray diffraction analysis, thermogravimetric analysis were carried out with the equipment from the resource centers of the St.-Petersburg State University Scientific park "Nanotechnology", "X-ray diffraction methods of research", "Thermogravimetric and calorimetric methods of research".

FUNDING

The reported study was supported by the Russian Foundation of Basic Research according to the research project no. 21-53-53012.

CONFLICT OF INTEREST

The authors declare that they have no conflict of interest.

INFORMATION ON THE AUTHORS' CONTRIBUTION

Authors M.A. Kamenskii, S.N. Eliseeva, and V.V. Kondratiev suggested the plan of the experiment and experimental procedures. A.Yu. Popov and M.A. Kamenskii synthesized specimens and studied their electrochemical properties, as well as are involved in the processing of the data. M.A. Kamenskii, S.N. Eliseeva, and V.V. Kondratiev are involved in the preparing the text. All authors are involved in the discussion of the results.

REFERENCES

1. Hwang, J.Y., Myung, S.T., and Sun, Y.K., Sodium-ion batteries: Present and future, *Chem. Soc. Rev.,* 2017, vol. 46, p. 3529.
2. Xie, J. and Zhang, Q., Recent progress in multivalent metal (Mg, Zn, Ca, and Al) and metal-ion rechargeable batteries with organic materials as promising electrodes, *Small,* 2019, vol. 15, p. 1805061.
3. Liang, Y., Dong, H., Aurbach, D., and Yao, Y., Current status and future directions of multivalent metal-ion batteries, *Nat. Energy,* 2020, vol. 5, p. 646.
4. Borchers, N., Clark, S., Horstmann, B., Jayasayee, K., Juel, M., and Stevens, P., Innovative zinc-based batteries, *J. Power Sources*, 2021, vol. 484, p. 229309.
5. Zhou, T., Zhu, L., Xie, L., Han, Q., Yang, X., Chen, L., Wang, G., and Cao, X., Cathode materials for aqueous zinc-ion batteries: A mini review, *J. Colloid Interface Sci.,* 2022, vol. 605, p. 828.
6. Selvakumaran, D., Pan, A., Liang, S., and Cao, G., A review on recent developments and challenges of cathode materials for rechargeable aqueous Zn-ion batteries, *J. Mater. Chem. A,* 2019, vol. 7, p. 18209.
7. Chen, L., An, Q., and Mai, L., Recent advances and prospects of cathode materials for rechargeable aqueous zinc-ion batteries, *Adv. Mater. Interfaces*, 2019, vol. 6, p. 1900387.
8. Mathew, V., Sambandam, B., Kim, S., Kim, S., Park, S., Lee, S., Alfaruqi, M.H., Soundharrajan, V., Islam, S., Putro, D.Y., Hwang, J-Y., Sun, Y-K., and Kim, J., Manganese and vanadium oxide cathodes for aqueous rechargeable zinc-ion batteries: a focused view on performance, mechanism, and developments, *ACS Energy Lett.,* 2020, vol. 5, p. 2376.
9. Guo, X., Yang, S., Wang, D., Chen, A., Wang, Y., Li, P., Liang, G., and Zhi, C., The energy storage mechanisms of MnO_2 in batteries, *Curr. Opin. Electrochem.,* 2021, vol. 30, p. 100769.
10. Zhang, Z., Li, W., Shen, Y., Wang, R., Li, H., Zhou, M., Wang, W., Wang, K., and Jiang, K., Issues and opportunities of manganese-based materials for enhanced Zn-ion storage performances, *J. Energy Storage,* 2022, vol. 45, p. 103729.
11. Post, J.E., Manganese oxide minerals: Crystal structures and economic and environmental significance, *Proc. Natl. Acad. Sci.,* 1999, vol. 96, p. 3447.
12. Jin, Y., Zou, L., Liu, L., Engelhard, M.H., Patel, R.L., Nie, Z., Han, K.S., Shao, Y., Wang, C., Zhu, J., Pan, H., and Liu, J., Joint charge storage for high-rate

aqueous zinc–manganese dioxide batteries, *Adv. Mater.,* 2019, vol. 31, p. 1900567.

13. Alfaruqi, M.H., Islam, S., Putro, D.Y., Mathew, V., Kim, S., Jo, J., Kim, S., Sun, Y-K., Kim, K., and Kim, J., Structural transformation and electrochemical study of layered MnO_2 in rechargeable aqueous zinc-ion battery, *Electrochim. Acta,* 2018, vol. 276, p. 1.
14. Li, G., Huang, Z., Chen, J., Yao, F., Liu, J., Li, O.L., Sun, S., and Shi, Z., Rechargeable Zn-ion batteries with high power and energy densities: A two-electron reaction pathway in birnessite MnO_2 cathode materials, *J. Mater. Chem. A,* 2020, vol. 8, p. 1975.
15. Wang, F., Lai, Y., Zhang, Y., Ou, P., Wu, P., Zhu, H., Chen, Z., and Li, S., Preparation of novel hollow δ-MnO_2 composite sphere for supercapacitors and degradation of bisphenol A, *Mater. Res. Bull.,* 2019, vol. 115, p. 257.
16. Wang, H., Liang, M., Gao, J., Ma, C., He, Z., Zhao, Y., and Miao, Z., Robust structural stability of flower-like δ-MnO_2 as cathode for aqueous zinc ion battery, *Colloids Surfaces A Physicochem. Eng. Asp.,* 2022, vol. 643, p. 128804.
17. Peng, H., Fan, H., Yang, C., Tian, Y., Wang, C., and Sui, J., Ultrathin δ-MnO_2 nanoflakes with Na^+ intercalation as a high-capacity cathode for aqueous zinc-ion batteries, *RSC Adv.,* 2020, vol. 10, p. 17702.
18. Egorova, A.A., Bushkova, T.M., Kolesnik, I.V., Yaprynstsev, A.D., Kottsov, S.Y., and Baranchikov, A.E., Selective synthesis of manganese dioxide polymorphs by the hydrothermal treatment of aqueous $KMnO_4$ solutions, *Russ. J. Inorg. Chem.*, 2021, vol. 66, p. 146.
19. Wu, Y., Fee, J., Tobin, Z., Shirazi-Amin, A., Kerns, P., Dissanayake, S., Mirich, A., and Suib, S.L., Amorphous manganese oxides: an approach for reversible aqueous zinc-ion batteries, *ACS Appl. Energy Mater.,* 2020, vol. 3, p. 1627.
20. Yang, X., Makita, Y., Liu, Z.H., Sakane, K., and Ooi, K., Structural characterization of self-assembled MnO_2 nanosheets from birnessite manganese oxide single crystals, *Chem. Mater.,* 2004, vol. 16, p. 5581.
21. Soundharrajan, V., Sambandam, B., Kim, S., Islam, S., Jo, J., Kim, S., Mathew, V., Sun, Y., and Kim, J., The dominant role of Mn^{2+} additive on the electrochemical reaction in $ZnMn_2O_4$ cathode for aqueous zinc-ion batteries, *Energy Storage Mater.,* 2020, vol. 28, p. 407.
22. Qiu, C., Zhu, X., Xue, L., Ni, M., Zhao, Y., Liu, B., and Xia, H., The function of Mn^{2+} additive in aqueous electrolyte for Zn/δ-MnO_2 battery, *Electrochim. Acta,* 2020, vol. 351, p. 136445.
23. Zhang, S., Liu, Z., Li, L., Tang, Y., Li, S., Huang, H., and Zhang, H., Electrochemical activation strategies of a novel high entropy amorphous V-based cathode material for high-performance aqueous zinc-ion batteries, *J. Mater. Chem. A,* 2021, vol. 9, p. 18488.
24. Zhang, Y., Huang, R., Wang, X., Wang, Z., Song, B., Du, Y., Lu, Q., Chen, X., and Sun, J., Facile large-scale preparation of vanadium pentoxide -polypyrrole composite for aqueous zinc-ion batteries, *J. Alloys Compd.,* 2022, vol. 907, p. 164434.
25. Huang, C., Wu, C., Zhang, Z., Xie, Y., Li, Y., Yang, C., and Wang, H., Crystalline and amorphous MnO_2 cathodes with open framework enable high-performance aqueous zinc-ion batteries, *Front. Mater. Sci.,* 2021, vol. 15, p. 202.
26. Liu, D-S., Mai, Y., Chen, S., Liu, S., Ang, E.H., Ye, M., Yang, Y., Zhang, Y., Geng, H., and Li, C.C., A 1D–3D interconnected δ-MnO_2 nanowires network as high-performance and high energy efficiency cathode material for aqueous zinc-ion batteries, *Electrochim. Acta,* 2021, vol. 370, p. 137740.
27. Huang, J., Wang, Z., Hou, M., Dong, X., Liu, Y., Wang, Y., and Xia, Y., Polyaniline-intercalated manganese dioxide nanolayers as a high-performance cathode material for an aqueous zinc-ion battery, *Nat. Commun.,* 2018, vol. 9, p. 2906.
28. Efremova, A.O., Volkov, A.I., Tolstopyatova, E.G., and Kondratiev, V.V., EQCM study of intercalation processes into electrodeposited MnO_2 electrode in aqueous zinc-ion battery electrolyte, *J. Alloys Compd.,* 2022, vol. 892, p. 162142.
29. Tan, Y., An, F., Liu, Y., Li, S., He, P., Zhang, N., Li, P., and Qu, X., Reaction kinetics in rechargeable zinc-ion batteries, *J. Power Sources,* 2021, vol. 492, p. 229655.
30. Zhang, R., Liang, P., Yang, H., Min, H., Niu, M., Jin, S., Jiang, Y., Pan, Z., Yan, J., Shen, X., and Wang, J., Manipulating intercalation-extraction mechanisms in structurally modulated δ-MnO_2 nanowires for high-performance aqueous zinc-ion batteries, *Chem. Eng. J.,* 2022, vol. 433, p. 133687.

Translated by Yu. Pleskov

SPELL: 1. ok